Use of commercial microwave links as scintillometers: potential and limitations towards evaporation estimation

Luuk D. van der Valk[1], Oscar K. Hartogensis[2], Miriam Coenders-Gerrits[1], Rolf W. Hut[1], Bas Walraven[1], and Remko Uijlenhoet[1]

[1]Department of Water Management, Delft University of Technology, Delft, the Netherlands
[2]Meteorology and Air Quality Group, Wageningen University & Research, the Netherlands

Correspondence: Luuk D. van der Valk (l.d.vandervalk@tudelft.nl)

Abstract. Scintillometers are used to measure path-integrated evaporation and sensible heat fluxes. They consist of a transmitter and a receiver separated along a line of sight of several hundreds of meters to a few kilometers. Turbulent eddies and the associated refractive index fluctuations along the path between transmitter and receiver cause diffraction of the transmitted beam, known as the scintillation effect. Optical and microwave scintillometers have been designed to measure the full spectral range of the signal intensity fluctuations caused by this phenomenon and quantitatively link these fluctuations to turbulent sensible- and latent heat fluxes. Commercial Microwave Links (CMLs), such as used in cellular telecommunication networks, are also line-of-sight instruments that measure signal intensity of microwave signals. However, CMLs are not designed to capture scintillation fluctuations. Here, we investigate if and under what conditions CMLs can be used to obtain the structure parameter of the refractive index, C_{nn}, which would be a first step in computing turbulent heat fluxes with CMLs using scintillation theory. We use data from three collocated microwave links installed over a 856 m path at the Ruisdael Observatory near Cabauw, the Netherlands. Two of these links are 38 GHz CMLs formerly employed in telecom networks in the Netherlands, a Nokia Flexihopper and an Ericsson MiniLink. We compare C_{nn} estimates obtained from the received signal intensity of these links, sampled at 20 Hz, with those obtained from measurements of a 160 GHz microwave scintillometer (RPG-MWSC) sampled at 1 kHz and of an eddy-covariance system. After comparison of the unprocessed C_{nn}, we rejected the Ericsson MiniLink, because its 0.5 dB power quantization (i.e., the discretization of the signal intensity) was found to be too coarse to be applied as a scintillometer. Based on power spectra of the Nokia Flexihopper and the microwave scintillometer, we propose two methods to correct for the white noise present in the signal of the Nokia Flexihopper: 1) we apply a high-pass filter and subtract the noise based on a comparison with the microwave scintillometer, and building on that 2) we select parts of the power spectra where the Nokia Flexihopper behaves in correspondence with scintillation theory, also considering different crosswind conditions, and correct for the underrepresented part of the scintillation spectrum based on theoretical scintillation spectra. The comparison and noise determination with the microwave scintillometer is provides the best possible C_{nn} estimates for the Nokia Flexihopper, although this is not feasible in operational settings for CMLs. Both of our proposed methods show an improvement of C_{nn} estimates in comparison to uncorrected estimates, albeit with a larger uncertainty than the reference instruments. Our study illustrates the potential of using CMLs as scintillometers, but also outlines some major drawbacks, most

25   of which are related to unfavourable design choices made for CMLs. If these would be overcome, given their global coverage, the potential of CMLs for large scale evaporation monitoring would be unprecedented.

1   Introduction

Surface turbulent heat fluxes play an important role in the energy and water cycles, where evaporation is connecting the two cycles. Observations of these surface fluxes can help improve our understanding of these land-atmosphere interactions and

30   advance our modelling capabilities (e.g., Wang and Dickinson, 2012) or serve as ground-truth for model simulations (e.g., Meir and Woodward, 2010; Seneviratne et al., 2010). Especially for evaporation, spatial estimates can provide essential information for catchment-scale water budgets and, for example, for irrigation requirements or drought monitoring (e.g., Burt et al., 2005; West et al., 2019). However, spatial estimates of actual evaporation with a high temporal and spatial resolution are difficult to obtain.

35   Traditionally, latent and sensible heat fluxes are measured with the eddy-covariance (EC) technique. This technique typically consists of a 3-D sonic anemometer and a fast-response hygrometer in order to determine the transport of momentum, temperature and moisture by using Reynolds decomposition. Spatial networks of EC systems are in operation, e.g., FLUXNET has over a 1000 active and historic sites, but lack the spatial coverage and density to be representative for all ecosystems and continents (e.g., Villarreal and Vargas, 2021). As an alternative, satellite remote sensing methods provide evaporation estimates with

40   improved spatial coverage, e.g., SEBAL (Bastiaanssen et al., 1998), SEBS (Su, 2002), MODIS (Mu et al., 2007) and ALEXI (Anderson et al., 1997). Drawbacks of these methods are that they either have a relatively low temporal or spatial resolution and that these are indirectly relating surface characteristics to evaporation under strong theoretical assumptions.

Other dedicated evaporation measurements can be performed with scintillometers, which make use of the scattering by turbulent eddies of electromagnetic radiation propagating through the atmosphere (e.g., Foken, 2021). As a consequence of the

45   different temperatures and humidities of turbulent eddies, density varies spatially and temporally and thus also the refractive index, causing the signal intensity at the receiving end of the propagation path to fluctuate in time (typically at time scales between 0.1 and 100 s). The signal intensity fluctuations detected by a scintillometer are related to the structure parameter of the refractive index, C_{nn}. Previous studies have shown that scintillometry can be used to estimate the turbulent heat fluxes (e.g., Kohsiek, 1982; Green et al., 2001). Moreover, Meijninger et al. (2002) showed that this measurement method is relatively

50   insensitive to land surface heterogeneity. However, scintillometers have mainly been used in dedicated field campaigns, because of the relatively high investment costs in installation and maintenance. To overcome the issues of spatiotemporal coverage and high investment costs, opportunistic sensing, where existing infrastructure is used for unintended purposes, could provide a wealth of information (e.g., de Vos et al., 2020).

Here, we explore opportunistic sensing with commercial microwave links (CMLs), which are near-surface terrestrial radio

55   connections used in cellular telecommunication networks, transmitting electromagnetic radiation with frequencies comparable to microwave scintillometers. Hence, in principle it should be possible to use CMLs as microwave scintillometers to estimate turbulent heat fluxes. CMLs are already used to estimate path-averaged rainfall rates by determining the rain-induced attenu-

ation along the link path (e.g., Messer et al., 2006; Leijnse et al., 2007a) and fog detection (David et al., 2013). Successfully using them as scintillometers would imply that CML signals could be used to estimate both fluxes that are part of the water balance (similar to Leijnse et al., 2007b, c). An additional benefit is that the infrastructure of these instruments already exists and is maintained by mobile network operators, also at locations where traditional measurements are lacking. Note that the number of operational CMLs worldwide is estimated to grow from 4.6 million in 2021 to 6 million in 2027 (ABI research, 2021).

In contrast to scintillometers, CMLs are not designed to monitor turbulent heat fluxes, as network operators are not interested in precisely monitoring high-frequency fluctuations in their networks. Most often network management systems store CML signal levels at too low temporal resolution, for example minimum and maximum values per 15 minutes, to capture the scintillation fluctuations. Additionally, the hardware of CMLs is not designed to measure scintillations. Some CMLs employ a coarse power quantization (i.e., the discretization of the signal intensity), as a result of choices in hardware as well as network management systems (e.g., Leijnse et al., 2008; Chwala et al., 2016; Ostrometzky et al., 2017). Moreover, in intercomparison studies (van Leth et al., 2018; van der Valk et al., 2024a), a formerly employed 38 GHz CML was found to exhibit a deviating behaviour in the high-frequency domain compared to a 38 GHz research link. Therefore, it is unclear whether CMLs could also be used to estimate C_{nn}, and thus potentially also the turbulent heat fluxes.

Here, we aim to explore the potential of using CMLs to estimate the turbulent heat fluxes by estimating C_{nn} based on fast (20 Hz) CML measurements and scintillation theory. We study how the CML signal behaves, to what extent it differs from what is expected from scintillation theory and how to correct for these differences. Between 11 September and 18 October 2023, we compared two 38 GHz CMLs with a 160 GHz microwave scintillometer, specifically designed to measure the turbulent heat fluxes, and an eddy-covariance system at the Ruisdael Observatory near Cabauw, the Netherlands. Both of these CMLs have formerly been employed in operational CML networks in the Netherlands. This allows us to study the overall potential of CMLs to estimate C_{nn} under relatively controlled conditions.

This paper is organized as follows: in Sect. 2, we provide a theoretical overview, in which we describe the state-of-the-art method required to obtain the turbulent heat fluxes using scintillation theory. In Sect. 3, we give an overview of our experimental setup and in Sect. 4, we show the initial C_{nn} estimates obtained with the CMLs when directly applying our CMLs as scintillometers. Based on this, we present our proposed correction methods to obtain C_{nn} estimates with CMLs in Sect. 5, partly based on the theory provided in Sect. 2. In Sect. 5.3, we show a verification of these proposed methods, followed by a discussion (Sect. 6) and conclusions (Sect. 7).

2 Theory

Here, we provide a brief overview of the theory required to obtain the turbulent heat fluxes with a focus on microwave links. For a more elaborate overview, see for example Foken (2021).

To relate the intensity fluctuations in the signal of a microwave scintillometer to the turbulent heat fluxes, the variance of the signal intensity per time interval has to be converted to the path-averaged structure parameter of the refractive index, C_{nn}

[m$^{-2/3}$]. Based on Tatarskiǐ (1961), Clifford (1971) proposed a theoretical model to relate the power spectrum of the signal intensity fluctuations to C_{nn}:

$$
S(f) = 4\pi^2 k^2 \int\limits_{0}^{1} \int\limits_{2\pi f u_\perp^{-1}}^{\infty} 0.033 C_{nn} K^{-8/3} \sin^2\left(\frac{K^2 L x (1-x)}{2k}\right)
$$

$$
\left((Ku_\perp(x))^2 - (2\pi f)^2\right)^{-1/2} \left(\frac{2J_1(0.5KD_\mathrm{R}x)}{0.5KD_\mathrm{R}x}\right)^2 \left(\frac{2J_1(0.5KD_\mathrm{T}(1-x))}{0.5KD_\mathrm{T}(1-x)}\right)^2 \mathrm{d}K\mathrm{d}x, \tag{1}
$$

in which $S(f)$ is the power spectrum, k [m^{-1}] is the wavenumber of the transmitted radiation (i.e., $k = 2\pi\lambda^{-1}$, in which

95   λ is the wavelength of the transmitted signal [m]), $u_\perp$ is the wind speed [m s^{-1}] perpendicular to the link path, f is the scintillation frequency [Hz], K [m^{-1}] is the turbulent wavenumber, L [m] is the path length, x [-] is the relative location along the link path, J_1 is the first-order Bessel function, and D_R and D_T [m] are the apertures of the receiver and transmitter, respectively. Typically, the 3D-power spectrum of the refractive index follows the power law $K^{-11/3}$ in the inertial subrange, following from the Kolmogorov law for three-dimensional turbulence spectra (Kolmogorov, 1941). For a power spectrum of

100   intensity measurements obtained from a scintillometer with a given setup, the power spectrum largely depends on C_{nn}, which increases the spectral density over the entire range of scintillation frequencies with higher C_{nn} values, and $u_\perp$, which shifts the scintillation spectrum to higher frequencies with higher $u_\perp$ values, while retaining the variance (e.g., Medeiros Filho et al., 1983; van Dinther, 2015).

Integrating Eq. (1) over f and analytically solving the integrals over K and x, yields a solution for the scintillation variance

105   (e.g., Hill and Ochs, 1978; Lüdi et al., 2005), which is independent of $u_\perp$ (e.g., Lawrence and Strohbehn, 1970; Tatarskii, 1971; Wang et al., 1978):

$$
C_{nn} = c\sigma^2_{\ln(I)} k^{-7/6} L^{-11/6}, \tag{2}
$$

in which c is a constant depending on the experimental setup (e.g., instrument characteristics and aperture averaging) and $\sigma^2_{\ln(I)}$ is the variance of the natural logarithm of the measured signal intensity. This relation is valid as long as the diameter of the

110   Fresnel zone (i.e., $F = \sqrt{\lambda L}$ [m]) is larger than the inner-scale length, l_0, and smaller than the outer-scale length, L_0. These are the length scales at which the turbulence spectrum transitions from inertial range to dissipation range and from production range to inertial range, respectively. For microwave links, this condition is usually valid (e.g., Ward et al., 2015). To obtain $\sigma^2_{\ln(I)}$, similar to Hartogensis (2006), it is common to first detrend, to prevent the introduction of fluctuations around the trend in the signal instead of turbulence, and normalise the natural logarithm of the signal intensity. Normalisation and applying a

115   high-pass filter (HPF), typically applied to remove signal intensity fluctuations as a result of absorption fluctuations, can both be done with a moving average of which the window size corresponds to the desired cut-off of the HPF.

C_{nn} is related to the structure parameters of temperature C_{TT} [K^2 m$^{-2/3}$], humidity C_{qq} [kg^2 kg^{-2} m$^{-2/3}$] and the cross-structure parameter C_{Tq} [K kg kg^{-1} m$^{-2/3}$], following (e.g., Foken, 2021):

$$
C_{nn} = \frac{A_T^2}{\overline{T}^2} C_{TT} + \frac{A_q^2}{\overline{q}^2} C_{qq} + 2\frac{A_T A_q}{\overline{T}\,\overline{q}} C_{Tq}, \tag{3}
$$

in which A_T and A_q are the structure parameter coefficients for temperature and specific humidity, respectively, $\overline{T}$ is the average temperature [K] and $\overline{q}$ is the average specific humidity [kg kg^{-1}]. Expressions for the temperature, humidity and pressure dependency of A_T and A_q are, for example, given in Ward et al. (2013). In order to determine the contributions of temperature and humidity fluctuations to the signal intensity fluctuations and relate these to the turbulent heat fluxes, most studies make use of two-wavelength scintillometry (though Leijnse et al., 2007b, used a microwave scintillometer in combination with a radiation budget constraint), in which two instruments operating at different wavelengths are combined. At optical wavelengths (i.e., $\lambda \approx 1\ \mu$m), the majority of the refractive index fluctuations are caused by temperature fluctuations, while for microwave wavelengths (i.e., $\lambda > 3$ mm) both temperature and humidity fluctuations contribute to the refractive index fluctuations.

Subsequently, the structure parameters can be converted to the turbulent heat fluxes using Monin-Obukhov Similarity Theory (MOST) (e.g., as proposed by Wyngaard et al., 1971):

$$H = \pm \rho c_{\mathrm{p}} K_{C_{TT}} z^{1/3} \sqrt{C_{TT}},$$

$$L_{\mathrm{v}}E = \pm \rho L_{\mathrm{v}} K_{C_{qq}} z^{1/3} \sqrt{C_{qq}}, \tag{4}$$

in which H is the sensible heat flux [W m^{-2}], $L_{\mathrm{v}}E$ is the latent heat flux [W m^{-2}], ρ is the air density [kg m^{-3}], c_{p} is the specific heat capacity of air [J kg^{-1} K^{-1}], L_{v} is the latent heat of vaporization [J kg^{-1}], $K_{C_{TT}}$ and $K_{C_{qq}}$ are exchange coefficients for temperature and humidity, respectively, and z is the measurement height [m]. In Appendix A, the derivation for $K_{C_{TT}}$ and $K_{C_{qq}}$ can be found.

3 Instrument and data description

3.1 Experimental setup

Our experiment is conducted using two commercial microwave links (CMLs), a microwave scintillometer (MWS) and an eddy-covariance system (EC) at the Ruisdael Observatory at Cabauw, the Netherlands (Fig. 1). The links and scintillometer transmit along an 856 meter path between 51.974252 N, 4.923484 E and 51.967552 N, 4.929561 E. On both sides, the CMLs and MWS are mounted on a 10 meter high vibration-free mast. The site is located in a marine west coast climate (Cfb in the Köppen classification). The water table is managed, so that the soil water content in the rootzone is kept as much as possible at field capacity (e.g., Brauer et al., 2014). The surrounding terrain consists mostly of grass fields and some small villages. Elevation differences in the area are within a few meters for distances up to more than 20 km (Ruisdael Observatory, 2024).
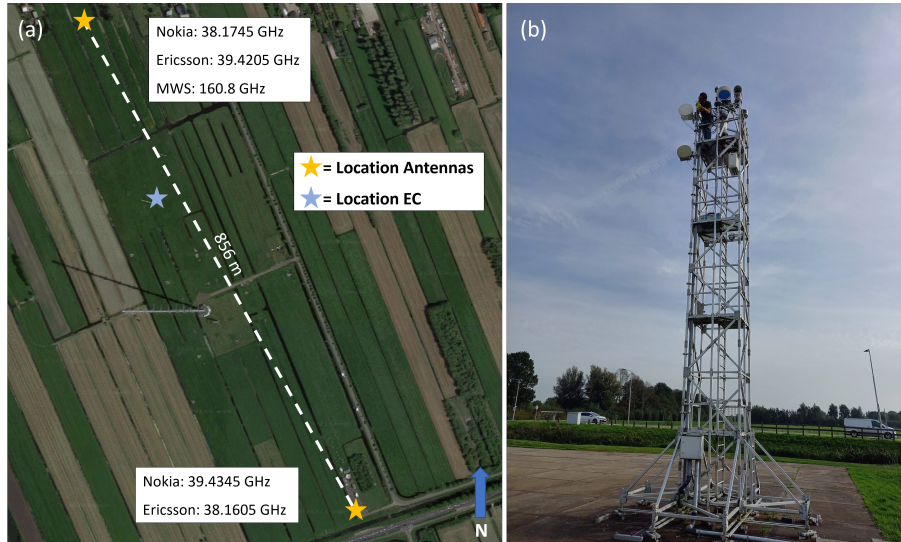
Figure 1. (a) Overview of CMLs, MWS and EC at the Ruisdael Observatory, Cabauw. Reported frequencies are the transmitting frequencies per antenna. (b) The southern mast with the 3 instruments installed. From top to bottom: the receiver of the MWS, the Nokia Flexihopper and the Ericsson MiniLink. (©Google maps)

3.2 Microwave Links

145 For this study, we use data of two collocated CMLs and an MWS. Both CMLs were formerly part of a commercial mobile phone network operated by T-Mobile Netherlands (currently, Odido Netherlands). These are a Nokia Flexihopper, mounted at 10 m above the surface, transmitting at 38.1745 GHz with a bandwidth of 0.9 MHz and an Ericsson MiniLink RAU2, mounted at 9 m above the surface, transmitting at 38.1605 GHz with a bandwidth of 7 MHz. Both links are bidirectional and transmit in the opposite direction at approximately 39.4 GHz. For this study, we only use the 38 GHz data (the 39 GHz data can be found

150 in van der Valk et al., 2024b). Both devices only transmit and receive horizontally polarized radiation.

Similar to van Leth et al. (2018), all signal intensities are sampled with a Campbell Scientific CR1000 datalogger at a 20 Hz sampling frequency. To sample the signal intensity, we direct the analogue detector signal used for automatic gain control to the datalogger. To convert the measured voltages to received signal intensities, we use the calibration curve provided by van Leth et al. (2018) for the Nokia Flexihopper:

$$I = -34.228V + 22.433, \tag{5}$$

in which V is the measured voltage [V] by the datalogger and I is the intensity [dB].

For the Ericsson MiniLink, the following standard equation is used (S. Gombert, employee Alfatech, personal communication, 04-06-2024):

$$I = -40V + 120. \tag{6}$$

160   The Nokia Flexihopper was installed on 11 September 2023 and the Ericsson MiniLink on 4 October 2023. We perform our analysis based on 30-minute time intervals, a typical time interval for turbulent heat fluxes (e.g., Green et al., 2001; Meijninger et al., 2002), until 18 October 2023. After this date (towards winter), the turbulent heat fluxes reduce, so that these are less clearly reflected in the C_{nn} estimates. For the Nokia Flexihopper, the transmitting 38 GHz antenna has been accidentally moved on 25 September, slightly reducing the received signal intensity. In order to account for this, we exclude this day from

165   our analysis and treat our data as two separate subsets, i.e., before and after this day.

   As a reference, we use a Radiometer Physics RPG-MWSC-160 microwave scintillometer, transmitting at 160.8 GHz, sampled at 1 kHz using the internal datalogger of the MWS. Data from the MWS is available during the entire period, with only minor data gaps, 1 hour per day at most. The MWS directly provides an analogue-to-digital converter level ranging between 0 and 65536 and proportional to signal intensity, which can be used in the subsequent analysis. The MWS is specifically designed

170   to measure the full spectral range of the signal intensity fluctuations caused by the scintillation effect and link these fluctuations to the turbulent heat fluxes.

   To compare the C_{nn} estimates obtained with the CMLs with the estimates from the MWS, we assume C_{nn} for 38 GHz and 160 GHz scintillation measurements to be the same, as suggested by the calculation proposed by Ward et al. (2013). Other studies suggest these values might slightly differ, though insignificantly in comparison to other uncertainties in our study. For

175   example using the analysis of Andreas (1989), for a sensible heat flux of 100 Wm^{-2} and a latent heat flux of 200 Wm^{-2} (and an air density of 1.2 kg m^{-3}, friction velocity of 0.2 ms^{-1}, relative humidity of 50 % and a temperature of 293 K), the C_{nn} for 38 GHz is 6.384×10^{-12} m$^{-2/3}$ and the C_{nn} for 160 GHz is 6.392×10^{-12} m$^{-2/3}$, a difference $\ll 1\%$ (based on the parameters of Kooijmans and Hartogensis, 2016).

   To allow for a comparison of the power spectra of the CMLs with the MWS, we convert the scintillation measurements of

180   the 160 GHz MWS to equivalent 38 GHz scintillation data. To do so, we need to transform the variance on the y-axis and the scintillation frequency of the MWS, i.e., the frequency on the x-axis in the power spectrum, $f_{\mathrm{MWS,160GHz}}$ (Clifford, 1971), i.e., a coordinate transformation which conserves variance. The variance can be transformed through Eq. (2). Following Clifford (1971), based on Eq. (1), the scintillation frequency is transformed as follows:

$$f_{\mathrm{MWS,38GHz}} = \frac{f_{\mathrm{norm,38GHz}}}{f_{\mathrm{norm,160GHz}}} \times f_{\mathrm{MWS,160GHz}}, \tag{7}$$

185   in which $f_{\mathrm{MWS,38GHz}}$ is the transformed frequency axis for the equivalent 38 GHz MWS data [Hz], f_{norm} [Hz] is commonly used to normalise the frequency axis (e.g., Clifford, 1971). The value of f_{norm} depends on transmitting frequency, hence the values for 38 GHz (i.e. $f_{\mathrm{norm,38GHz}}$) and 160 GHz (i.e. $f_{\mathrm{norm,160GHz}}$) differ. To compute f_{norm}, the following equation is used

$$f_{\mathrm{norm}} = u_{\perp}(2\pi\lambda L)^{-1/2}, \tag{8}$$

190   which reduces the fraction in Eq. (7) to $\sqrt{38/160} = 0.4873$. Hereafter, when referring to the MWS data, we refer to the equivalent 38 GHz MWS data.

   Additionally, we smooth the power spectra similar to Hartogensis (2006). To do so, each point in the power spectrum is smoothed by averaging it with the neighbouring points in a specified window. We specify the window as 20% of the position

of the to be smoothed data point. The weighting of these points within the window is assumed to be bell-shaped, so that the
195 adjacent points have more influence on the smoothing than the points at the far end of the window.

After studying the Ericsson link time series and variances, we decided to exclude this link from this scintillometry analysis.
The 0.5 dB power quantization of the device prevents us from obtaining representative variances. Graphs of the time series and
variances of the Ericsson link are available in the Appendix B. For the influence of power quantization on $\sigma^2_{\ln(I)}$ of the Nokia
link, see Appendix C.

200 For our analysis we do not consider nighttime time intervals (i.e., incoming shortwave radiation below 50 W m^{-2}), intervals
during which it rained or those that follow within an hour after a rain event (to exclude wet-antenna attenuation in our analysis),
and intervals with absolute wind speed above 8 m s^{-1}. The latter is applied because the Nokia CML vibrates above this wind
speed, as we observe in our data an increase in variances above this limit (not shown). Additionally, for our corrected C_{nn}
estimates (Sect. 5), we remove all time intervals with C_{nn} estimates larger than 6.49×10^{-12} m$^{-2/3}$, which we expect to be
205 the maximum value for our dataset. Using Eqs. (3) and (4), this value is based on the assumption that 80 % of the maximum
incoming shortwave radiation (i.e., approximately 800 W m^{-2} for this dataset) is used for the turbulent heat fluxes with a
minimum Bowen ratio (which results in a maximum C_{nn}) of 0.2 (and an air density of 1.2 kg m^{-3}, friction velocity of 0.2 m
s^{-1}, a temperature of 293 K and a specific humidity of 0.015 kg kg^{-1}).

3.3 Eddy Covariance data

210 EC measurements are used to compute additional independent C_{nn} estimates. The EC system consists of a sonic anemometer
(Gill-R50) and an open-path H$_2$O/CO$_2$ sensor (LICOR-7500) and is installed at 3 meter above the ground (Bosveld et al.,
2020). The measurement frequency of the system is 10 Hz.

To estimate C_{nn} with EC measurements, we compute C_{TT}, C_{qq} and C_{Tq} from the raw temperature and humidity measure-
ments, defined as (e.g., Stull, 1988),

$$215 \quad C_{yy} \equiv \frac{\overline{(y(x) - y(x+r))^2}}{r^{2/3}} = \frac{\overline{(y(t) - y(t+\Delta t))^2}}{(\overline{u}\Delta t)^{2/3}}, \tag{9}$$

in which $y(x)$ is either T or q at location x and r [m] is a separation distance. To estimate structure parameters from time series,
Taylor's frozen turbulence hypothesis has to be assumed, so that $y(x)$ is replaced by $y(t)$, which is either T or q at timestep
t [s], and r has been replaced by the mean horizontal wind speed $\overline{u}$ multiplied with Δt. Additionally, we have to correct for
the height difference between the EC measurements (i.e., 3 m) and the links (i.e., 10 m), as the structure parameters are not
220 constant with height, in contrast to the turbulent heat fluxes. To do so, we use Eqs. A1 to A4 in Appendix A.

It should be noted that the temperature and raw wind speed components for the EC show unexpected behaviour, because
some temperatures and wind speeds are more frequently measured than adjacent temperatures and wind speeds (See Fig.
S1 for a histogram of the wind speed, temperature and humidity measurements during a full day, i.e., 11 september 2023).
However, the overall behaviour of these components does not show any abnormalities. Therefore, we expect this only has a
225 minor influence on the C_{TT}, C_{qq}, u_* and H calculations, the latter two required in Eq. (A5).

For our analysis, we also make use of other meteorological measurements at Cabauw (available from KNMI Data Platform), such as air temperature, humidity, wind speed, precipitation and radiation. The majority of these measurements are needed for the conversion of the MWS data to 38 GHz (e.g., $u_\perp$) and to correct the Nokia CML variances (Sect. 5).

3.4 Error Metrics

230 In this study, we compare C_{nn} estimates of the various instruments. For all comparisons, we use the the relative mean bias error (RMBE), the 10-90 interquantile range (IQR) and Pearson's correlation coefficient (r). For all metrics, we use the logarithmic values of the C_{nn} estimates, since C_{nn} typically exhibits a log-normal distribution throughout the day (e.g., Kohsiek, 1982; Green et al., 2001). The RMBE is calculated as:

$$\text{RMBE} = \overline{\log(y) - \log(x)}, \tag{10}$$

235 in which $\log$ indicates the decimal logarithm, y are the C_{nn} estimates of the instrument on the y-axis and x are the C_{nn} estimates of the instrument on the x-axis, i.e., the reference instrument. Intuitively, the RMBE represents the orders of magnitude the values on the y-axis are larger (or smaller) than the reference values on the x-axis. The IQR is calculated as follows:

$$\text{IQR} = P_{90} - P_{10}, \tag{11}$$

in which P_{90} and P_{10} are the 90th and 10th percentiles of the difference between the logarithmic C_{nn} estimates of the instrument
240 on the y-axis and the logarithmic C_{nn} estimates of the instrument on the x-axis of a scatterplot. The IQR can be interpreted as how many orders of magnitude the 90th percentile of the residuals is larger than the 10th percentile of the residuals. For r, we use the logarithmic values of the C_{nn} estimates, so that this value visually corresponds to the correlation on a log-log plot.

4 CML C_{nn} estimates without correction procedure

An initial comparison of C_{nn} estimates, without any correction, between the Nokia CML and the MWS shows a systematic
245 overestimation by the Nokia CML in comparison to the MWS (Fig. 2). Additionally, outliers are especially present in the C_{nn} estimates of the Nokia CML. Generally, the reference instruments, i.e., MWS and EC, show good agreement (Fig. 3).
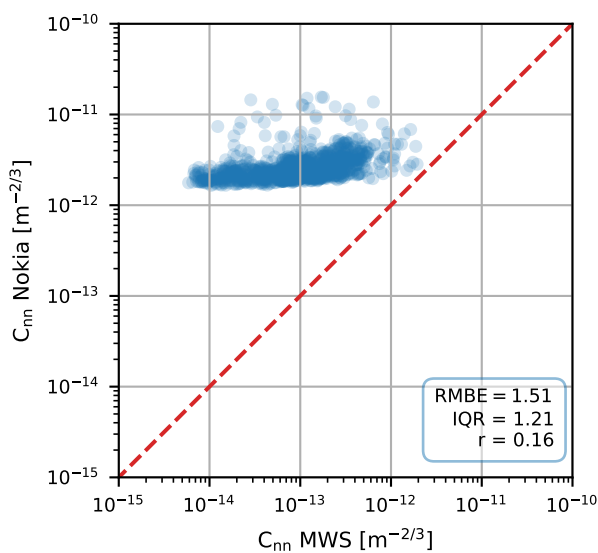
Figure 2. 30-min C_{nn} estimates obtained with the unprocessed Nokia CML data versus the MWS. The red dashed line is the 1:1 line.
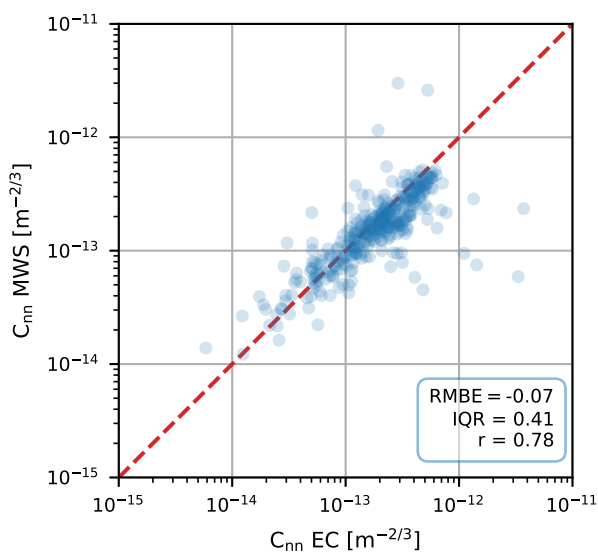
Figure 3. 30-min C_{nn} estimates obtained with the MWS versus the EC, corrected for the height difference (Sect. 3.3). The red line is the 1:1 line.

When zooming in on example power spectra of the Nokia CML and MWS signal intensities (Fig. 4), the MWS behaves as expected based on theory and shows in the scintillation part of the spectrum ($f > 10^{-1}$ Hz) a decrease with a constant slope on

log-log scale, similar to the theoretical spectrum (Sect. 2). Yet, there is a minor difference between the MWS and theory, most

250 likely as a consequence of an underestimation of the path-averaged crosswind speeds. These crosswinds shift the scintillation spectrum towards higher frequencies with higher crosswind speeds, but retain the variance (e.g., see van Dinther, 2015). The Nokia CML shows, in the scintillation part of the spectrum, a deviating behaviour from the MWS, as no decrease with increasing frequencies is found. Additionally, in this specific case, the Nokia CML seems to be more susceptible to absorption fluctuations compared to the MWS, as reflected by the increased power spectrum values at low frequencies ($f < 10^{-1}$ Hz), at

255 which absorption fluctuations typically occur (e.g., Medeiros Filho et al., 1983).

The differences in the scintillation part of the spectrum can be explained by considering a spectrum during which the transmitting antenna had been turned off (Fig. 5). With no signal transmitted, the Nokia CML receiver registers a white noise signal. Figures 4 and 5 combined demonstrate that the total $\sigma^2_{\ln(I)}$ consists of, in addition to scintillations and absorption fluctuations, a large white noise signal that explains the large C_{nn} overestimation seen in Fig. 2. In general, this shows that

260 the white noise is the biggest limitation to obtain reasonable C_{nn} estimates using the Nokia CML. The noise present in the received signal intensity aligns with the typical noise floor in radio receivers (e.g., Friis, 1944). The designed noise floor usually depends on the intended application. Moreover, the values of these noise floors are often not publicly (fully) available. For our study, and in a broader sense for determining evaporation using CMLs, noise complicates the retrieval process and requires a practical solution. In Sect. 5, we present two methods to correct the C_{nn} estimates using the Nokia CML for the presence of

265 noise.
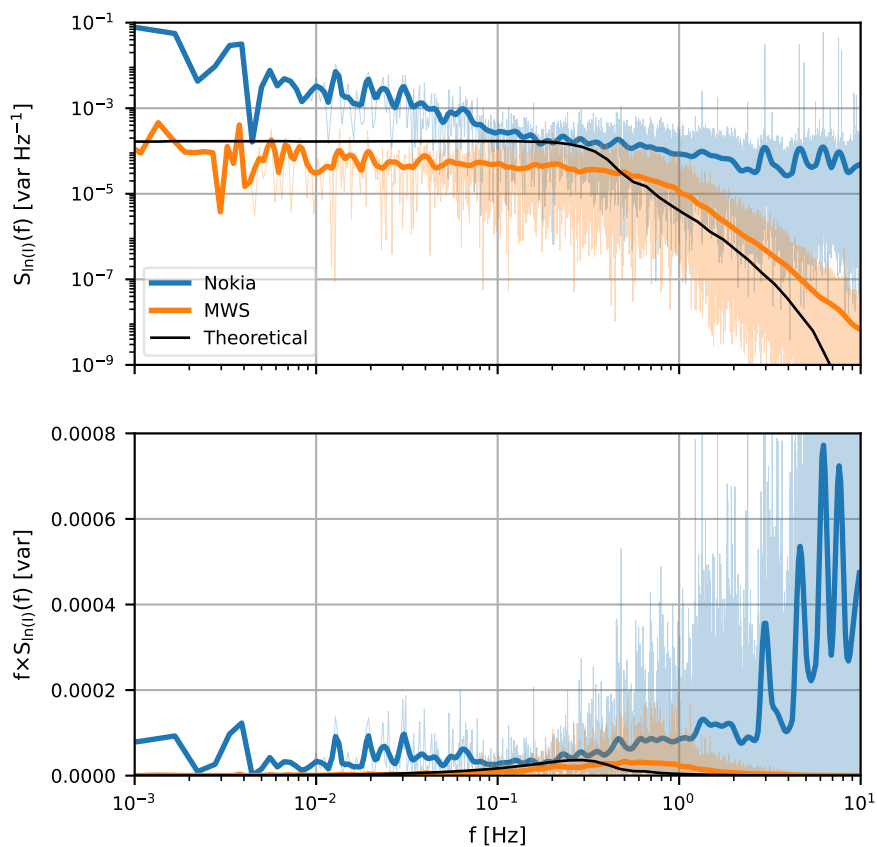
Figure 4. (a) Power spectrum of the signal intensities of the MWS (orange), Nokia CML (blue) and a theoretical spectrum, using C_{nn} obtained with the MWS, of a theoretical 38 GHz MWS based on Eq. (1) on 12-09-2023 between 9:00 and 9:30 UTC and (b) the contribution to the variance of the signal intensity per logarithmic frequency interval. The shaded areas are the raw power spectra, while the lines are the smoothed versions of the spectra (following Hartogensis, 2006). Note that the MWS in this case is the equivalent 38 GHz MWS data (Eq. 7 in Sect. 3.2).
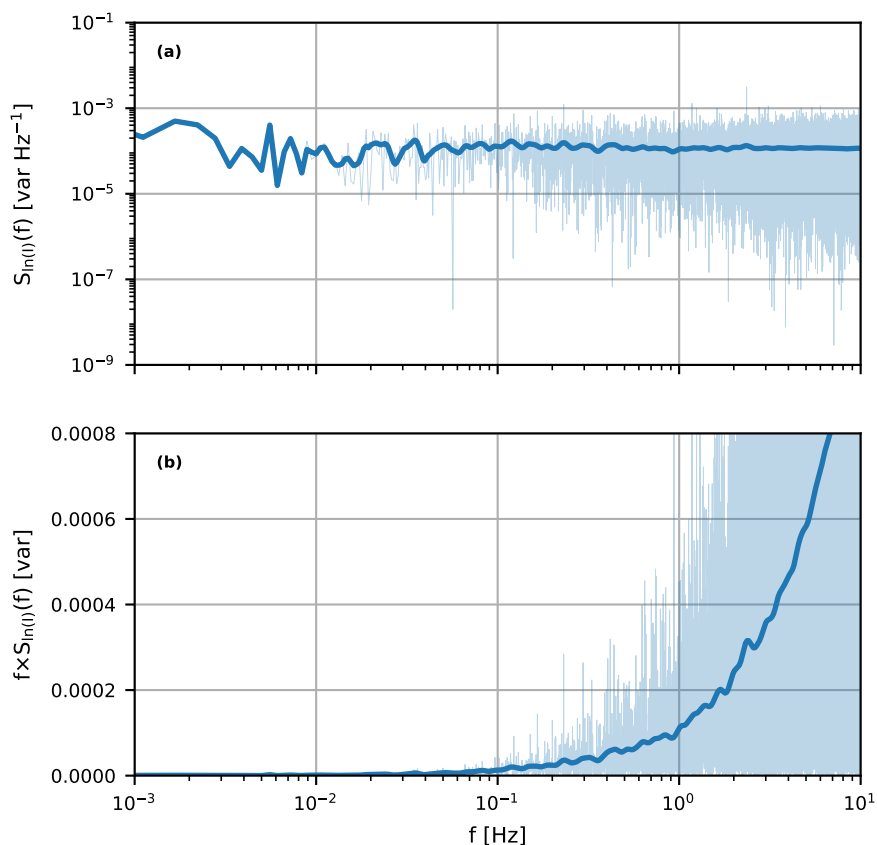
Figure 5. (a) Power spectrum of the signal intensities of the Nokia CML on 25-11-2023 between 13:00 and 13:30 UTC, during which the transmitting antenna was turned off and (b) the contribution to the variance of the signal intensity per logarithmic frequency interval. The shaded areas are the raw power spectra, while the line is the smoothed versions of the spectra (following Hartogensis, 2006).

5   CML C_{nn} estimates with correction procedure

In this section, we provide two practical correction methods for the observed deviating parts in the power spectra of the Nokia CML. Both methods make use of a form of spectral cleaning. The first method is a basic noise correction based on the overall difference in variance between the Nokia CML and the MWS, assuming that noise always has the same influence on the scintillation signal. In reality, as remarked previously, the scintillation part of the power spectrum shifts to higher frequencies with higher crosswinds (e.g., Foken, 2021; van Dinther, 2015), so that for high crosswinds the scintillation spectra overlap more with the noise-dominated part of the spectrum. Therefore, we refer to this method as *crosswind-independent*. Our second method builds on the crosswind-independent correction method, but also considers the influence of crosswind conditions on the power spectra. We select parts of the power spectra where the Nokia CML corrected with the first method behaves

275 in correspondence with the MWS, dependent on crosswind conditions, and correct for the omitted part of the scintillation spectrum based on scintillation theory.

5.1 Method 1: Crosswind-independent noise correction

Our first method assumes there is a constant noise floor present in the Nokia CML signal, probably as a consequence of the designed noise floor in the receiving antenna, and no or negligible noise is present in the MWS (Figs. 4 and 5). Under these

280 assumptions, we can write the variances as:

$$\sigma^2_{\text{MWS}} = \sigma^2_{absorption} + \sigma^2_{scintillations},$$
$$\sigma^2_{\text{CML}} = \sigma^2_{\text{MWS}} + \sigma^2_{noise}. \tag{12}$$

The method consists of estimating the contribution of the noise floor to $\sigma^2_{\ln(I)}$ by subtracting the MWS-derived from the Nokia CML-derived value of $\sigma^2_{\ln(I)}$ (Eq. 12). We determine the noise floor in the high-frequency range (1-10 Hz) of the power spectra (Fig. 4), where the noise has the largest influence on the spectrum and the influence of scintillations is relatively low, and

285 convert these levels to the complete power spectra.

Step 1. Noise estimation

    (a) ***Filter out absorption:*** For each time interval, we apply a high-pass filter at 0.1 Hz, by subtracting the moving average with a window size of 10 s from the signal intensity time series. Effectively this filters out the gray area in Fig. 6.
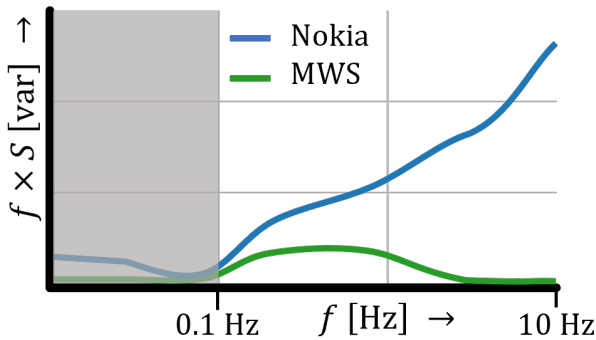
Figure 6. Step 1a: Hypothetical power spectrum with application of a high-pass filter at 0.1 Hz to the Nokia CML (blue) and the MWS (green).

290   (b) ***Subsample power spectrum in noise region:*** In this method, the region between the CML and MWS for $f >$ 1 Hz is assumed to be dominated by noise and contain a low contribution from scintillations (Fig. 4), which is especially valid for relatively low crosswind speeds based on theory (Fig. D1). For each time interval, we compute the average S per 0.2 log(f) spectral bin between 1 and 10 Hz for both devices (Fig. 7a), so that we capture the

average behaviour of the noise in the Nokia CML without being largely affected by incidental peaks (Fig. 4b). Per

295 bin, we subtract the S for the MWS from S for the Nokia CML, resulting in S_{noise} per bin for each time interval.

We take the median of all spectral bins and time intervals resulting in an estimate of S_{noise} between 1 and 10 Hz

for all time intervals (Fig. 7), hereafter denoted as $\widetilde{S}_{noise}$.
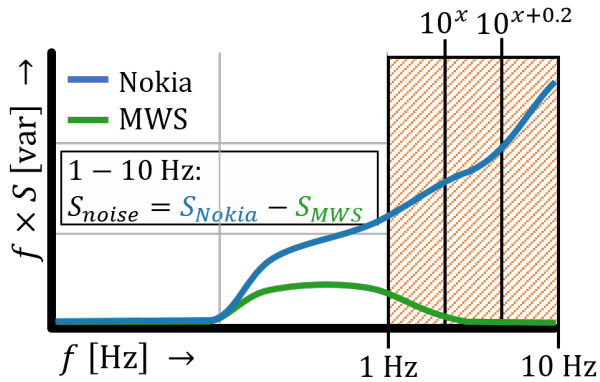
Figure 7. Step 1b: S_{noise} calculation between 1 and 10 Hz per 0.2 $\log(f)$ spectral bin for the Nokia CML (blue) and MWS (green) for $f \times S$ spectrum.

(c) ***Determine*** σ^2_{noise}***:*** We assume the noise in the Nokia CML is independent of f, given that it is white noise (Fig.

5a). Thus, we can determine σ^2_{noise} between 0.1 (the applied high-pass filter cutoff) and 10 Hz from $\widetilde{S}_{noise}$ over

300 all time intervals between 1 and 10 Hz (Fig. 8), as determined in the previous step. To do so, we make use of the

definition to compute variances from power spectra, so that,

$$\sigma^2_{noise} = \int_{0.1Hz}^{10Hz} \widetilde{S}_{noise} \, \mathrm{d}(f) = \int_{\ln(0.1Hz)}^{\ln(10Hz)} f \times \widetilde{S}_{noise} \, \mathrm{d}\ln(f). \tag{13}$$

This results in $\sigma^2_{noise} = 6.53 \times 10^{-4}$ (i.e., $C_{nn,noise} = 2.31 \times 10^{-12}$ m$^{-2/3}$) between 0.1 and 10 Hz before the

movement of the transmitting Nokia antenna (Sect. 3.2) and $\sigma^2_{noise} = 5.23 \times 10^{-4}$ (i.e., $C_{nn,noise} = 1.85 \times 10^{-12}$

305 m$^{-2/3}$) between 0.1 and 10 Hz after movement, indicating that the added noise is signal intensity- dependent.
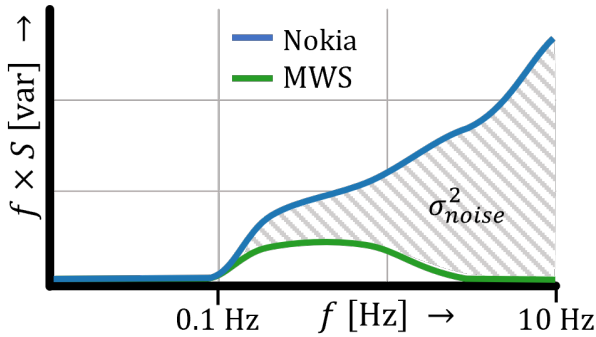
Figure 8. Step 1c: Converting $\widetilde{S}_{noise}$ between 1 and 10 Hz to σ^2_{noise} between 0.1 and 10 Hz by applying Eq. (13).

Step 2. Noise correction application to obtain C_{nn}

(a) ***Subtract*** σ^2_{noise}***:*** In order to obtain a corrected $\sigma^2_{\ln(I)}$, we subtract the σ^2_{noise} from $\sigma^2_{\ln(I)}$ for the high-pass filtered Nokia CML for all time intervals.

(b) ***Clean noise-corrected*** $\sigma^2_{\ln(I)}$***:*** Due to the noise determination in step 1b, it is possible that negative $\sigma^2_{\ln(I)}$ values occur as well, whereas variances should be positive by definition. Therefore, we remove all time intervals with negative corrected $\sigma^2_{\ln(I)}$ for the Nokia CML, i.e., 17 % of the available time intervals for this method.

(c) ***Compute*** C_{nn}***:*** For each time interval, we compute C_{nn} estimates from the corrected and cleaned $\sigma^2_{\ln(I)}$ (Eq. 2).

5.2   Method 2: Crosswind-dependent noise correction

In this method, we build on the crosswind-independent correction method, but taking into account the crosswind condition, as the scintillation spectrum shifts to higher frequencies with higher crosswind speeds. We therefore select, depending on the crosswind, those parts of the spectrum where the Nokia CML and the MWS data behave similarly. For example, in Fig. 4b between approximately 0.1 and 1 Hz, the Nokia CML and the MWS show a relatively similar behaviour, especially after applying the noise correction obtained in Sect. 5.1. After computing the (partial) variance of the selected parts of the spectrum, we correct for the fraction of $\sigma^2_{\ln(I)}$ omitted based on the theoretical spectra (Eq. 1).

Step 1. Noise estimation

(a) ***Subsample spectra:*** Similar to step 1b in Sect. 5.1, for each time interval, we compute the variance per $0.2 \log(f)$ spectral bin, but now between 0.01 and 10 Hz for both devices (Fig. 7a). For the Nokia CML, we subtract per bin σ^2_{noise} determined in step 1b in Sect. 5.1 by converting these to the corresponding frequency bin, similar to Eq. (13).

(b) ***Determine frequency range over which Nokia CML resolves scintillations:*** We assume the corrected Nokia CML resolves part of the scintillations. Therefore, we establish a frequency range in which the Nokia CML behaves in correspondence with the MWS. We determine for the whole dataset the frequency bins for which the CML and

MWS spectrum are in close agreement as a function of crosswind. To this end, we separate the dataset in crosswind classes between 0 and 5 m s^{-1} with class sizes of 1 m s^{-1}. Within each crosswind class, frequency bins are deemed

330 similar when they meet the following criteria over all timesteps: a) they should contain more than 50 observations, and b) both the RMBE and IQR of $\sigma^2_{\ln(I)}$ should have values below 1 (Fig. 9). This is done to make sure we have a representative sample size of observations per wind class which does not differ, on average, more than one order of magnitude in comparison to the MWS estimates. The resulting frequency ranges can be found in Table 1.
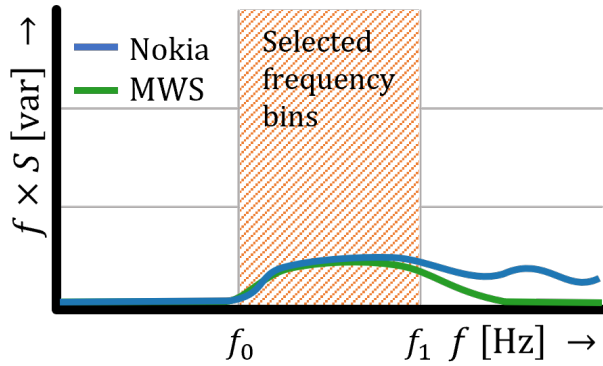
Figure 9. Step 1b: Selected frequency bins for an individual power spectrum by comparing the Nokia CML corrected using the crosswind-independent method (blue) with the MWS (green).

(c) ***Transfer function for omitted part of the power spectrum:*** By selecting parts of the power spectra, we have to
335 correct for the omitted part of the spectrum. Therefore, we determine a transfer function that corrects for the spectral contribution of scintillations outside the selected frequency bins for which the Nokia CML agrees well with the MWS (Fig. 10). We do this per crosswind class using the theoretical spectrum (Eq. 1). To compute what fraction the $\sigma^2_{\ln(I)}$ of the selected parts of the spectrum represent, Eq. (1) only requires k (i.e., a function of f), $u_\perp$ and D. C_{nn} does not affect this fraction, as it only affects the variance (i.e., the area below the scintillation
340 spectrum) and not the location in the frequency domain. This results in a transfer function TF,

$$\text{TF} = \frac{\int_{-\infty}^{\infty} f \times S_{theory}\, \text{dln}(f)}{\int_{\ln(f_0)}^{\ln(f_1)} f \times S_{theory}\, \text{dln}(f)}, \tag{14}$$

of which f_0 and f_1 depend on crosswind conditions and can be found in Table 1 and S_{theory} in this case refers to the theoretical power spectrum (Eq. 1). The values for the transfer function are shown in Fig. 11. For $u_\perp$, we use the exact value and not the crosswind class values, so that within each class the value of the transfer function still
345 varies, especially for the lowest crosswind speeds. Note that the large shifts in values for TF between crosswind classes are a consequence of the different total width of the selected frequency bins of the power spectrum (Table 1). The size of the selected frequency bins for crosswind classes 1-2 m s^{-1} and 4-5 m s^{-1} are smaller than the other classes, so that the value for TF becomes relatively large.
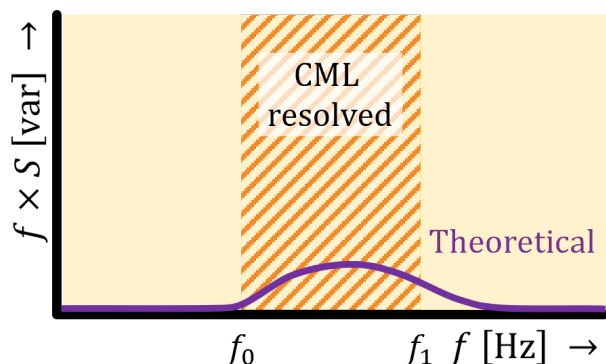
Figure 10. Step 1c: Theoretical spectrum in which red hatched area indicates the selected frequency bins based on step 1b (i.e., the denominator in Eq. 14) and the orange area indicates the full frequency axis (i.e., the numerator in Eq. 14). f_0 and f_1 depend on crosswind conditions and can be found in Table 1.

Table 1. Lower, f_0, and upper, f_1, bound of spectra with an RMBE and IQR below 1 and more than 50 observations per crosswind class. Note that values for f_0 and f_1 are written as decimal logarithm in this table, while Eq. 14 makes use of the bounds written as natural logarithms to compute TF.

$u_\perp$ class [m s^{-1}]	f_0 [log(Hz)]	f_1 [log(Hz)]
0 - 1	-1.8	-0.2
1 - 2	-1.2	0.0
2 - 3	-1.6	0.0
3 - 4	-1.4	0.2
4 - 5	-0.4	0.2
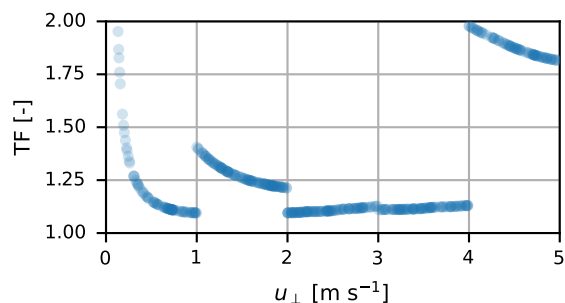
Figure 11. The values of the Transfer Function TF (Eq. 14) as function of crosswind $u_\perp$.

Step 2. Noise correction application to obtain C_{nn}

350

(a) ***Compute total*** $\sigma^2_{\ln(I)}$***:*** To determine the $\sigma^2_{\ln(I)}$ as a result of scintillations, we integrate for each time interval the $\sigma^2_{\ln(I)}$ of the selected parts of the spectrum (step 1b, Table 1), depending on crosswind class, and multiply these values with the corresponding transfer function (Eq. 14).

(b) ***Clean noise-corrected*** $\sigma^2_{\ln(I)}$***:*** Due to the noise determination in step 1b in Sect. 5.1, it is possible that negative $\sigma^2_{\ln(I)}$ values occur as well, whereas variances should be positive by definition. Therefore, we remove all time

355

intervals with negative corrected $\sigma^2_{\ln(I)}$ for the Nokia CML, i.e., 7 % of the available time intervals for this method.

(c) ***Compute*** C_{nn}***:*** For each time interval, we compute C_{nn} estimates from the corrected and cleaned $\sigma^2_{\ln(I)}$ (Eq. 2).

5.3 Performance of the two correction methods
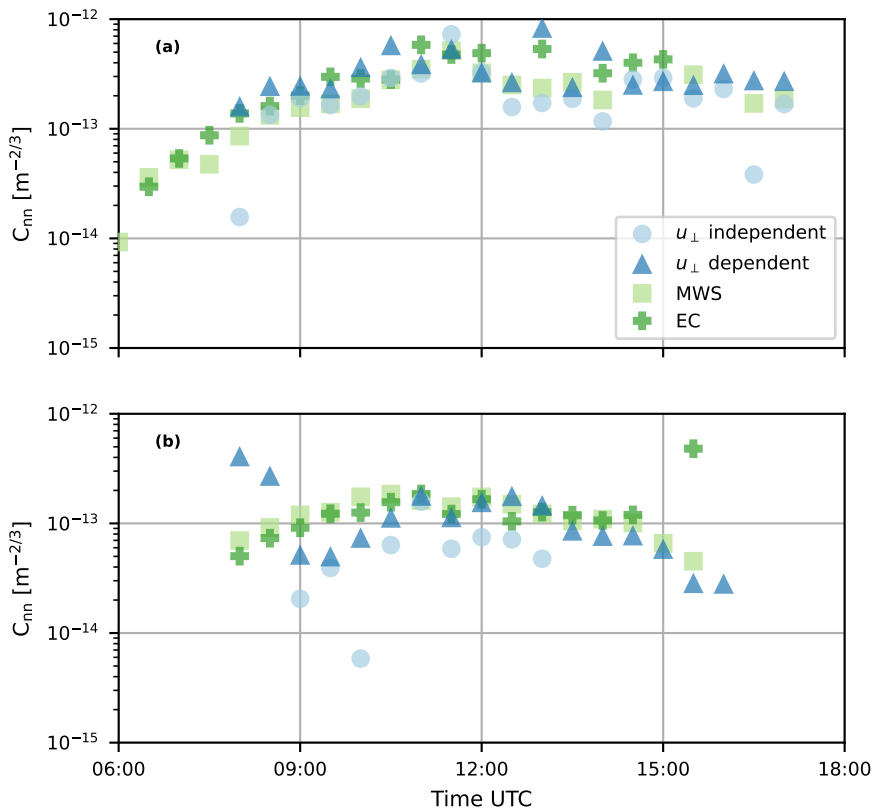
Figure 12. Time series with 30-min C_{nn} estimates on (a) a sunny day, 14 September 2023, and (b) a cloudy day, 9 October 2023.

Time series of a sunny day versus a cloudy day (Figs. 12a and b), show both methods capture the daily cycle typically found in C_{nn} estimates, but with some more outliers compared to the reference instruments. Similar to the reference instruments, the

360 C_{nn} estimates of our corrections are generally higher on the sunny day than on the cloudy day. The crosswind-independent

method shows more outliers than the crosswind-dependent method, and also contains more time intervals with lacking C_{nn} estimates, especially during the cloudy day. The latter is partly a consequence of the noise determination (Step 3 in Sect. 5.1), which corrects the lowest C_{nn} estimates to negative values, which have been removed. Note that on the cloudy day, the time series starts 2 hours later than on the sunny day and ends 1 hour earlier, because we removed all time intervals with a downward

365 solar radiation less than 50 W m^{-2}. Moreover, relatively high crosswind speeds during the cloudy day cause the noise region of the Nokia CML to dominate over the scintillation spectrum, causing an additional effect on the performance of the crosswind-independent method. During the cloudy day crosswind speeds range between 2 and 4 m s^{-1}, while for the sunny day these are around 1 m s^{-1}, so that the scintillation spectrum is shifted to higher frequencies on the cloudy day, causing the noise to overlap with the scintillation spectrum. On the sunny day, with relatively high C_{nn} estimates combined with low crosswind speeds,

370 both methods perform more similarly, though still show an occasional outlier.
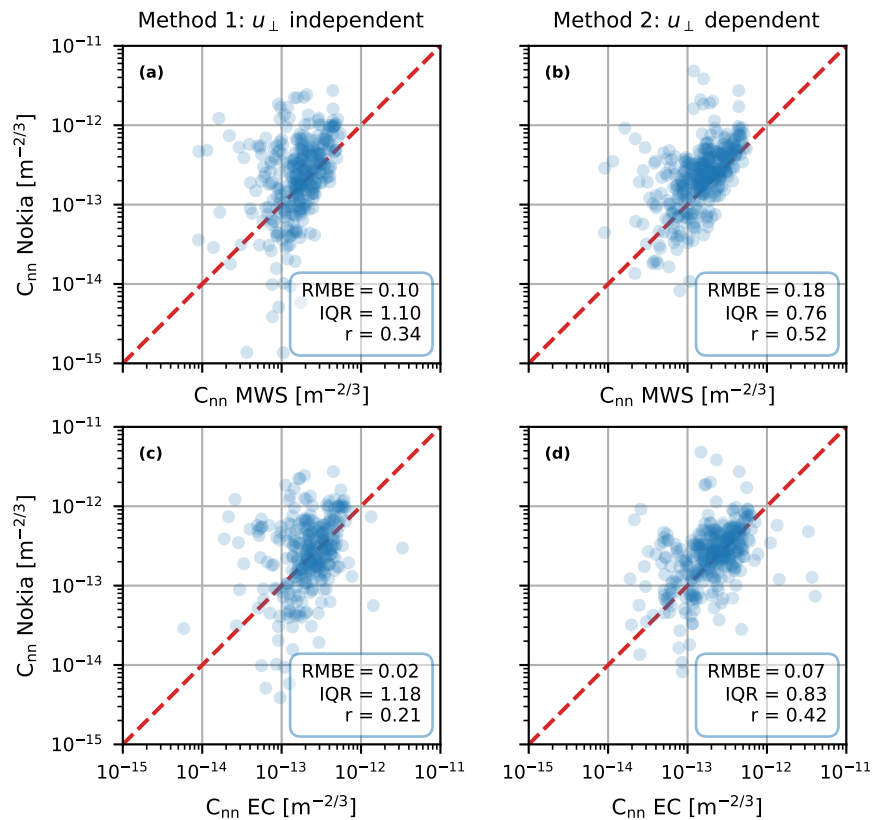
Figure 13. 30-min C_{nn} estimates obtained with the Nokia CML for the entire study period, post-processed with the crosswind-independent method (a and c) and crosswind-dependent method (b and d) versus the MWS (a and b) and the EC (c and d) estimates, corrected for the height difference (Sect. 3.3). The red line is the 1:1 line.

For our entire dataset, both proposed methods show a huge improvement (Fig. 13) in comparison to the unprocessed Nokia CML C_{nn} estimates (Fig. 2). The RMBE related to both the MWS and EC has reduced from 1.5 to at least 0.18, which

is comparable to the RMBE of the comparison between the reference instruments (i.e., -0.07), indicating that the proposed methods overestimate C_{nn} at most with a factor 1.5 (i.e., $10^{0.18}$). Also, both our proposed methods increase the correlation

375   coefficient, especially the crosswind-dependent method. Moreover, the crosswind-dependent method reduces the IQR to at least 0.83, while the crosswind-independent method does not show any reduction in comparison to the IQR of the unprocessed C_{nn} estimates (i.e., 1.21). This is a consequence of the nature of our corrections, as the crosswind-independent method only removes noise, but does not affect the spread of the data, while the crosswind-dependent method considers the IQR during the selection of parts of the power spectrum (step 3 in Sect. 5.2). It should be noted that for the crosswind-independent method,

380   small C_{nn} values have a tendency to be underestimated while large C_{nn} values are overestimated, which is also reflected in the time series (Fig. 12). This is caused by the noise determination (step 3 in Sect. 5.1) for which we use the difference between the Nokia CML and the MWS in the scintillation part of the spectrum. This behaviour is not found for the crosswind-dependent method, because the parts of the spectrum with the largest influence of the noise on $\sigma^2_{\ln(I)}$, and thus possibly the parts resulting in large underestimations, have been filtered out (i.e., $f > 1$ Hz; Table 1).

385   **6   Discussion**

This study aims to explore the potential and limitations of using CMLs as microwave scintillometers. Our study is an idealized experiment, as we use 20 Hz data from two 38 GHz CMLs formerly employed by a mobile network operator in The Netherlands and are able to compare these CMLs with a dedicated 160 GHz microwave scintillometer. Even though this does not match the common sampling strategy of CMLs in telecommunication networks, it enables us to perform a detailed study. We initially

390   focus on estimating the structure parameter of the refractive index C_{nn} using CMLs, as this is a key feature in the workflow to obtain the turbulent heat fluxes with scintillation theory.

6.1 C_{nn} estimates using CMLs

As a proof of concept, our results show that, under certain conditions, CMLs could be used to estimate C_{nn}, though with a larger uncertainty and bias with respect to both reference instruments, an MWS and EC, than the comparison between the

395   reference instruments among each other. Our two proposed methods to correct the Nokia CML scintillation spectra and obtain C_{nn} estimates show a comparable behaviour, though the crosswind-dependent method outperforms the crosswind-independent method, especially regarding the spread. An advantage of the crosswind-independent method is that it is a relatively simple correction method which does not require predetermining those parts of the spectrum behaving similarly to the MWS. However, the crosswind-independent method underestimates low C_{nn} values, which is not the case for the crosswind-dependent method.

400   Overall, this shows that considering crosswind conditions, affecting the location of the power spectrum on the frequency axis, also improves the C_{nn} estimation. However, it also requires a more elaborate study of the power spectrum of the CML and the MWS, which might not always be possible.

Both methods require an MWS to determine the contribution of noise to C_{nn}, which limits the ability to transfer our methods to other datasets. When an MWS is available to install next to a CML, both our methods can be used to estimate C_{nn} using

405   CMLs, under the condition that the noise in the CML is of a similar nature as the noise in the Nokia CML. This even holds for different experimental conditions, such as other path lengths or installation heights, since these are indirectly accounted for in our methods. The only difficulty might arise when the contribution of noise to the signal intensity fluctuations is relatively large in comparison to the scintillation fluctuations. Moreover, when assuming the noise is caused by a stationary white noise floor in the receiving antenna (e.g., Friis, 1944), installing an MWS next to the CML would even not be required for a full

410   experimental period, but it would be sufficient to perform a one-time determination of the noise floor, possibly even for a single type of CML.

    However, usually an MWS is not available to install next to a CML, let alone an entire network of CMLs. Even application of our instruments to different experimental conditions without an MWS would probably cause difficulties. For the crosswind-independent method, an alternative to overcome this issue and determine the noise could be to assume that the minimum C_{nn}

415   (or a low percentile) in the dataset is equivalent to the noise contribution to C_{nn}, so that this minimum C_{nn} value can be subtracted from the entire dataset (due to the proportionality between C_{nn} and $\sigma_{\ln(I)}^2$, see Eq. 2). Moreover, for other CML types most often it will be required to have a collocated MWS, in order to determine the nature of the signal, including the noise. Having full information in advance on the introduction of noise in the receiving antenna of CMLs would allow for a more precise correction of the noise, possibly not even requiring the use of an MWS. For example, this could disclose the

420   dependency of a noise floor on the signal intensity or the possible presence of any frequency-domain filter. Yet, usually this information is not shared publicly, complicating the C_{nn} estimation.

    Previous scintillometer studies confirm the obtained correspondence between microwave scintillometer C_{nn} estimates and in-situ EC measurements. Herben and Kohsiek (1984), who built on Kohsiek and Herben (1983), reported C_{nn} estimates with a 30 GHz scintillometer at 60 meter above the surface showing a similar behaviour as C_{nn} estimates obtained with

425   high-frequency temperature, humidity and wind measurements. Similarly, Hill et al. (1988) showed that C_{nn} measurements performed by a 173 GHz scintillometer only slightly underestimated C_{nn} estimates obtained with EC high-frequency meteorological measurements. Similarly, Beyrich et al. (2005) and Ward et al. (2015), reported C_{TT}, C_{qq} and C_{Tq} estimates from an EC system which were comparable to measurements from a dual-beam scintillometer setup (optical and microwave). Hence, compared to previous studies our C_{nn} estimates from CMLs exhibit a relatively large uncertainty.

430   Other studies have tried to estimate C_{nn} using meteorological observations in order to complement lacking C_{nn} observations. Van de Boer et al. (2014) used single-level observations to obtain the energy balance and used the Penman-Monteith equation to estimate C_{nn}. A comparison of their simulated C_{nn} estimates with EC-based C_{nn} estimates over grassland seems to outperform our comparison between CML and EC estimates, though their method shows a large dependence on the quality of the meteorological input data. Similarly, Tunick (2003) estimated C_{nn} using two-level meteorological observations of wind

435   speed, temperature and humidity. Also, Andreas (1988) provided C_{nn} estimates over snow and ice by using meteorological observations and emphasized the strong dependence of his estimates on the non-linear relation between the fluxes and C_{nn} and the dependence on the assumed Bowen ratio. Even though some of these studies outperform our C_{nn} estimates, these all require high-quality meteorological input data, which are not often available, whereas C_{nn} estimates obtained from CML signal

intensities would be a more direct method to obtain C_{nn}, do not require any additional measurements and have a potentially

440   larger global coverage.

6.2   The potential of using CMLs as scintillometers

Several aspects of CML networks could prevent obtaining similar C_{nn} estimates, as CMLs are not designed to measure the scintillations. Firstly, power quantization affects the measured variances of signal intensity. From the used devices, a Nokia and an Ericsson CML, we rejected the Ericsson CML to estimate C_{nn} using scintillation theory, because of 0.5 dB power quan-

445   tization (i.e., the discretization of the signal intensity). Power quantization is a commonly applied method in CML networks, typically ranging between 0.1 and 1 dB (Chwala and Kunstmann, 2019). Based on our data, we have the impression that for the smallest quantization steps, C_{nn} estimates could still be feasible, though it would be an additional source of uncertainty (Fig. C1a and b).

Secondly, the CMLs have not been designed with the aim to measure scintillations, which is also reflected by the presence

450   of noise in signal intensity of the Nokia CML. To correct for this inability to capture the scintillations, we determined our noise levels with the MWS, which usually is not possible for a CML. In order to determine how antennas modify the received signal intensity, a comparison with an MWS would be required for each specific type of CML antenna before being able to estimate C_{nn} or having full information on the noise. Moreover, the mounting mechanism of the CMLs is not designed to be vibration free, as the Nokia CML started to vibrate above 8 m s^{-1}, even though the mast itself remained free of vibrations.

455   Thirdly, typical temporal sampling strategies applied in CML networks are on a coarser temporal resolution than our 20 Hz sampling. Typically, CML signal intensities are stored in the network management system every 15 minutes with minimum and maximum values of the signal intensity (and occasionally also with a mean intensity included). Another sampling strategy, developed by Chwala et al. (2016), allows to select an instantaneous sampling strategy with time intervals as small as 1 s, of which variances might approach actual signal variances (Fig. C1c). Our selected 20 Hz sampling strategy mimics the typical

460   instantaneous sampling strategy on which the coarser sampling strategies are based. However, it could be that adding the variance to the operationally reported signal intensities is relatively easy, as calculating the variance is only one additional computation from calculating the mean value per time interval.

This study focused on obtaining C_{nn} estimates, while to compute the turbulent heat fluxes additional information, and thus uncertainty, on the distribution between temperature and humidity fluctuations is required. For scintillometer setups, an

465   optical link is usually collocated next to the MWS. The optical link is mostly sensitive to temperature fluctuations (and can also be used to solely determine the sensible heat flux), so that the structure parameter of humidity can be extracted from the C_{nn} estimates by the MWS. For (the vast majority of) CMLs, no in-situ measurements are available, complicating the required separation between the temperature and humidity structure parameters. To do so, it would be required to use global meteorological data, such as satellite measurements or model data, but it is questionable how accurate and useful this would

470   be to eventually retrieve the turbulent heat fluxes. Either way, the required assumptions in this computation step introduce additional uncertainty, possibly making the overall uncertainty in the turbulent heat fluxes relatively large. In a follow-up study, we will focus on obtaining the turbulent heat fluxes from the presented methods to estimate C_{nn}. As a potential solution

to reduce the relatively large uncertainties, we will look into the influence of upscaling the 30-min estimates to daily estimates. Additionally, we aim to use a more extensive dataset (around a full year), instead of 37 days in September and October, to

475   identify potential influences of other weather circumstances on obtaining C_{nn} estimates.

7 Conclusions

In this study, we explored the potential of using CMLs as scintillometers based on a dataset with two formerly employed CMLs, an MWS (all collocated) and an EC system along the link path. We focused on obtaining C_{nn} estimates using CMLs collecting 20 Hz data, as scintillation theory requires C_{nn} to be able to compute the turbulent heat fluxes.

480   An initial comparison of the Nokia Flexihopper and the MWS showed an overestimation of C_{nn}, due to the addition of white noise over the signal intensity. To correct for this, we propose two methods: 1) Applying a high-pass filter and subtracting the noise in the high-frequency ranges of the power spectrum, determined by a comparison with the MWS (resulting in the best possible estimates); 2) building on the correction in the first method, selecting parts of the power spectrum in which the Nokia CML behaves similar to the MWS and scintillation theory, also considering different crosswind conditions, and correct for the

485   lacking scintillations based on scintillation theory. Both proposed methods show a huge improvement in terms of the RMBE and correlation coefficient with respect to the MWS and EC estimates compared to uncorrected C_{nn} estimates, while the second method also improves the IQR by selecting the best performing parts of the power spectra. However, these values are still larger than the RMBE, IQR and correlation coefficient between the MWS and the EC, and also appear larger than C_{nn} estimates from previous studies using meteorological data. On the other hand, C_{nn} estimates from CMLs provide a more direct

490   measurement of C_{nn} with a potentially large global coverage.

We rejected the Ericsson MiniLink to estimate C_{nn} due to the power quantization present in the signal, which is common for part of the CMLs. This illustrates that some of the challenges faced when estimating C_{nn} are a consequence of design choices made for CMLs. Next to power quantization and the noise found in the Nokia CML, CMLs are usually not mounted on vibration-free masts (or the mounts of the CMLs are not vibration-free), so that under specific wind conditions the antennas

495   could start to vibrate. Additionally, typical temporal sampling strategies in CML network management systems are on a coarser temporal resolution than our 20 Hz sampling. Yet, having network management systems to report also the variance per time interval could be an effective measure, which would not require much more computational memory than the mean signal already reported by some networks. More in general, our proposed methods both require the presence of a collocated reference scintillometer, which is obviously not possible for each CML, possibly not even for each type of CML.

500   In general, our study illustrates the potential to use CMLs as scintillometers, but also illustrates some of the major challenges, especially as a result of the design choices made for CMLs. A clear next challenge is to obtain the turbulent heat fluxes from these C_{nn} estimates, if possible without the need for elaborate additional meteorological measurement data. Additionally, more comparisons of CMLs with MWSs are required to estimate the potential of other CML types, also in other climatic settings, and assess the overall potential of CMLs as scintillometers. Lastly, an attempt could be made to directly retrieve information

505   on the turbulent heat fluxes from the received signal intensities without following the scintillation theory, but for example using

statistical methods or machine learning, as, in the end, the received signal of CMLs is just as much affected by turbulent eddies as the signal of a MWS.

Data availability. The MWS and CML data can be found at van der Valk et al. (2024b). KNMI data can be dowloaded from https://dataplatform.knmi.nl/ (KNMI Data Platform). The raw EC data has been acquired directly from KNMI via opendata@knmi.nl.

510 **Appendix A: Derivation of the exchange coefficients $K_{C_{TT}}$ and $K_{C_{qq}}$**

The exchange coefficient for temperature $K_{C_{TT}}$ and humidity $K_{C_{qq}}$ can be derived using Monin-Obukhov Similarity Theory (MOST). The structure parameters C_{TT} and C_{qq} can be related to the turbulent temperature T_* [K] and humidity scales q_* [kg kg^{-1}],

$$\frac{C_{TT} z^{2/3}}{\overline{T}_*^2} = f_{TT}\left(\frac{z}{L_{\mathrm{Ob}}}\right),$$
$$\frac{C_{\mathrm{qq}} z^{2/3}}{\overline{q}_*^2} = f_{qq}\left(\frac{z}{L_{\mathrm{Ob}}}\right), \tag{A1}$$

515 in which L_{Ob} is the Obukhov length [m], and f_{TT} and f_{qq} are universal functions.

The turbulent heat fluxes are directly related to T_* and q_*:

$$T_* = -\frac{H}{\overline{\rho} c_{\mathrm{p}} u_*},$$
$$q_* = \frac{(1-\overline{q}) L_{\mathrm{v}} E}{\overline{\rho} L_{\mathrm{v}} u_*}, \tag{A2}$$

in which c_{p} is the specific heat capacity of air [J kg^{-1} K^{-1}], u_* is the friction velocity [m s^{-1}] and L_{v} is the latent heat of vaporization [J kg^{-1}]. Subsequently, $K_{C_{TT}}$ and $K_{C_{qq}}$ can be calculated as,

$$K_{C_{TT}} = u_* f_{TT}^{-1/2},$$
520 $$K_{C_{qq}} = u_* (1-\overline{q})^{-1/2} f_{qq}^{-1/2}. \tag{A3}$$

Kooijmans and Hartogensis (2016) define the universal functions f_{TT} and f_{qq} for unstable conditions as

$$f_{TT} = 5.6\left(1 - 6.5\frac{z}{L_{\mathrm{Ob}}}\right)^{-2/3},$$
$$f_{qq} = 4.5\left(1 - 7.3\frac{z}{L_{\mathrm{Ob}}}\right)^{-2/3}, \tag{A4}$$

in which the parameter values are based on a large comparison study. L_{Ob} is defined as

$$L_{\mathrm{Ob}} = -\frac{\overline{\rho} c_{\mathrm{p}} \overline{T} u_*^3}{g \kappa H}, \tag{A5}$$

525 in which g is the gravitational acceleration [m s^{-2}] and κ is the von-Karmán constant.

Appendix B: Results for the Ericsson MiniLink
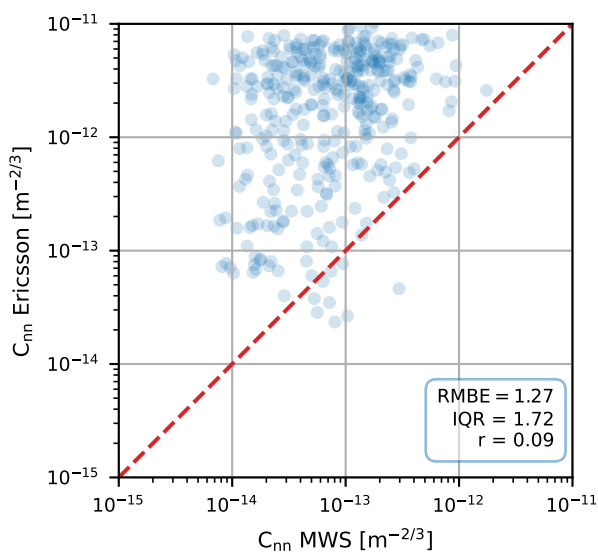
Figure B1. 30-min C_{nn} estimates obtained with the Ericsson MiniLink data versus the MWS. The red dashed line is the 1:1 line. Note that the data has not been cropped, but has a maximum C_{nn} value around 10^{-11} m$^{-2/3}$.
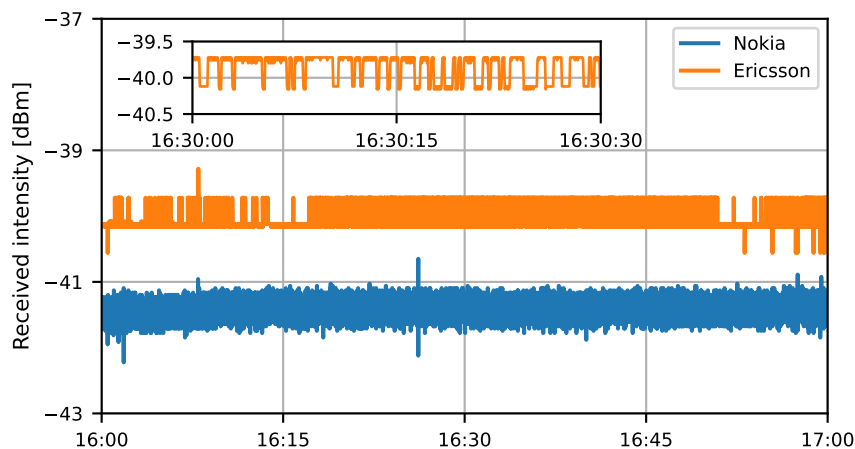
Figure B2. Timeseries of received signal intensity for Nokia Flexihopper and Ericsson MiniLink on 5 October 2023. The inset graph shows a 30 second snapshot of the Ericsson timeseries.

Appendix C: Influence of quantization and temporal sampling on signal intensity variance
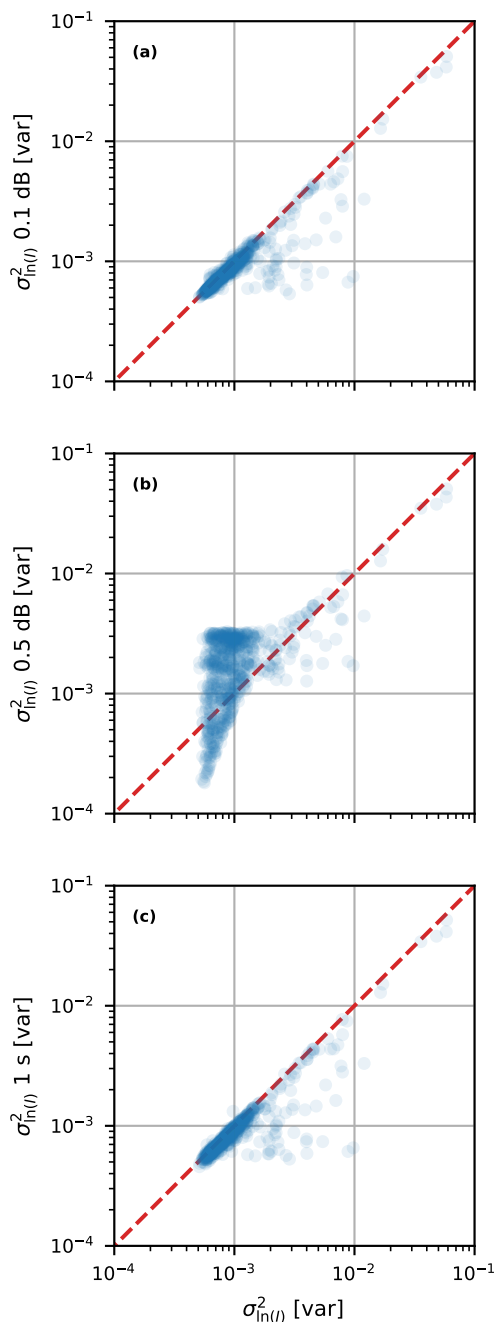
Figure C1. 30-min $\sigma^2_{\ln(I)}$ obtained with Nokia CML data with 0.1 dB power quantization (a), Nokia CML data with 0.5 dB power quantization (b) and 1 second Nokia CML data (c) versus the original 20 Hz Nokia CML data. The red dashed line is the 1:1 line.

Appendix D: Theoretical captured fraction below 1 Hz for Nokia
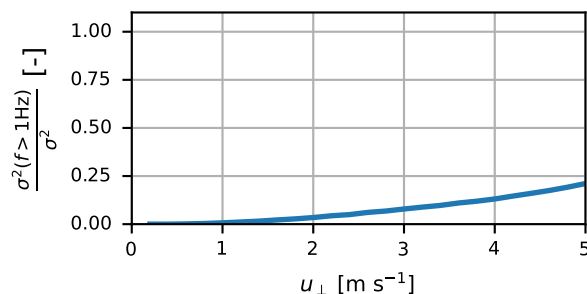
Figure D1. Theoretical fraction of the total variance due to scintillations occurring above 1 Hz for the Nokia CML as function of crosswind speed $u_\perp$. These are derived from the theoretical spectrum in Eq. (1) using the characteristics of the Nokia CML.

Author contributions. LDvdV carried out the research under the supervision of OKH, MCG, RWH, and RU. LDvdV performed the field
530   experiment together with BW. LDvdV prepared the manuscript, with contributions from all co-authors.

Competing interests. The authors declare that they have no competing interests

Acknowledgements. This manuscript has been accomplished by using (data generated in) the Ruisdael Observatory, a scientific research
infrastructure which is (partly) financed by the Dutch Research Council (NWO, grant number 184.034.015).

References

ABI research: Wireless Backhaul Evolution Delivering Next-Generation Connectivity, https://www.gsma.com/spectrum/wp-content/uploads/2022/04/wireless-backhaul-spectrum.pdf [Accessed: 30-01-2024], 2021.

Anderson, M. C., Norman, J. M., Diak, G. R., Kustas, W. P., and Mecikalski, J. R.: A two-source time-integrated model for estimating surface fluxes using thermal infrared remote sensing, Remote Sensing of Environment, 60, 195–216, https://doi.org/https://doi.org/10.1016/S0034-4257(96)00215-5, 1997.

Andreas, E. L.: Estimating C_n^2 over snow and sea ice from meteorological data, Journal of Optical Society of America, 5, 15, https://doi.org/https://doi.org/10.1364/JOSAA.5.000481, 1988.

Andreas, E. L.: Two-wavelength method of measuring path-averaged turbulent surface heat fluxes, Journal of Atmospheric and Oceanic Technology, 6, 280–292, https://doi.org/10.1175/1520-0426(1989)006<0280:Twmomp>2.0.Co;2, 1989.

Bastiaanssen, W. G. M., Menenti, M., Feddes, R. A., and Holtslag, A. A. M.: A remote sensing surface energy balance algorithm for land (SEBAL). 1. Formulation, Journal of Hydrology, 212-213, 198–212, https://doi.org/10.1016/S0022-1694(98)00253-4, 1998.

Beyrich, F., Kouznetsov, R. D., Leps, J.-P., Lüdi, A., Meijninger, W. M., and Weisensee, U.: Structure parameters for temperature and humidity from simultaneous eddy-covariance and scintillometer measurements, Meteorologische Zeitschrift, 14, 641–649, https://doi.org/10.1127/0941-2948/2005/0064, 2005.

Bosveld, F. C., Baas, P., Beljaars, A. C. M., Holtslag, A. A. M., de Arellano, J. V.-G., and van de Wiel, B. J. H.: Fifty Years of Atmospheric Boundary-Layer Research at Cabauw Serving Weather, Air Quality and Climate, Boundary-Layer Meteorology, 177, 583–612, https://doi.org/10.1007/s10546-020-00541-w, 2020.

Brauer, C. C., Torfs, P. J. J. F., Teuling, A. J., and Uijlenhoet, R.: The Wageningen Lowland Runoff Simulator (WALRUS): application to the Hupsel Brook catchment and the Cabauw polder, Hydrology and Earth System Sciences, 18, 4007–4028, https://doi.org/10.5194/hess-18-4007-2014, 2014.

Burt, C. M., Mutziger, A. J., Allen, R. G., and Howell, T. A.: Evaporation Research: Review and Interpretation, Journal of Irrigation and Drainage Engineering, 131, 37–58, https://doi.org/10.1061/(asce)0733-9437(2005)131:1(37), 2005.

Chwala, C. and Kunstmann, H.: Commercial microwave link networks for rainfall observation: Assessment of the current status and future challenges, WIREs Water, 6, https://doi.org/10.1002/wat2.1337, 2019.

Chwala, C., Keis, F., and Kunstmann, H.: Real-time data acquisition of commercial microwave link networks for hydrometeorological applications, Atmospheric Measurement Techniques, 9, 991–999, https://doi.org/10.5194/amt-9-991-2016, 2016.

Clifford, S. F.: Temporal-frequency spectra for a spherical wave propagating through atmospheric turbulence, JOSA, 61, 1285–1292, 1971.

David, N., Alpert, P., and Messer, H.: The potential of commercial microwave networks to monitor dense fog-feasibility study, Journal of Geophysical Research: Atmospheres, 118, 11,750–11,761, https://doi.org/10.1002/2013jd020346, 2013.

de Vos, L. W., Droste, A. M., Zander, M. J., Overeem, A., Leijnse, H., Heusinkveld, B. G., Steeneveld, G. J., and Uijlenhoet, R.: Hydrometeorological Monitoring Using Opportunistic Sensing Networks in the Amsterdam Metropolitan Area, Bulletin of the American Meteorological Society, 101, E167–E185, https://doi.org/10.1175/bams-d-19-0091.1, 2020.

Foken, T.: Springer handbook of atmospheric measurements, https://doi.org/10.1007/978-3-030-52171-4, 2021.

Friis, H. T.: Noise figures of radio receivers, Proceedings of the IRE, 32, 419–422, 1944.

Green, A., Astill, M., McAneney, K., and Nieveen, J.: Path-averaged surface fluxes determined from infrared and microwave scintillometers, Agricultural and Forest Meteorology, 109, 233–247, https://doi.org/10.1016/S0168-1923(01)00262-3, 2001.

Hartogensis, O.: Exploring scintillometry in the stable atmospheric surface layer, Ph.D. thesis, Wageningen University and Research, ISBN 9798516028625, 2006.

Herben, M. H. A. J. and Kohsiek, W.: A comparison of radio wave and in situ observations of tropospheric turbulence and wind velocity, Radio Science, 19, 1057–1068, https://doi.org/10.1029/RS019i004p01057, 1984.

575 Hill, R. J. and Ochs, G. R.: Fine calibration of large-aperture optical scintillometers and an optical estimate of inner scale of turbulence, Applied Optics, 17, 3608–3612, https://doi.org/10.1364/AO.17.003608, 1978.

Hill, R. J., Bohlander, R. A., Clifford, S. F., McMillan, R. W., Priestly, J. T., and Schoenfeld, W. P.: Turbulence-induced millimeter-wave scintillation compared with micrometeorological measurements, IEEE Transactions on Geoscience and Remote Sensing, 26, 330–342, https://doi.org/10.1109/36.3035, 1988.

580 KNMI Data Platform: KNMI Data Platform, https://dataplatform.knmi.nl/ [Accessed: 03-01-2024].

Kohsiek, W.: Measuring C_T^2, C_Q^2 and C_{TQ} in the unstable surface layer, and relations to the vertical fluxes of heat and moisture, Boundary-Layer Meteorology, 24, 89–107, https://doi.org/10.1007/BF00121802, 1982.

Kohsiek, W. and Herben, M.: Evaporation derived from optical and radio-wave scintillation, Applied optics, 22, 2566–2570, https://doi.org/10.1364/AO.22.002566, 1983.

585 Kolmogorov, A. N.: The local structure of turbulence in incompressible viscous fluid for very large Reynolds numbers, In Dokl. Akad. Nauk SSSR, 30, 301, 1941.

Kooijmans, L. M. J. and Hartogensis, O. K.: Surface-layer similarity functions for dissipation rate and structure parameters of temperature and humidity based on eleven field experiments, Boundary-Layer Meteorology, 160, 501–527, https://doi.org/10.1007/s10546-016-0152-y, 2016.

590 Lawrence, R. S. and Strohbehn, J. W.: A survey of clear-air propagation effects relevant to optical communications, Proceedings of the IEEE, 58, 1523–1545, https://doi.org/10.1109/PROC.1970.7977, 1970.

Leijnse, H., Uijlenhoet, R., and Stricker, J. N. M.: Rainfall measurement using radio links from cellular communication networks, Water Resources Research, 43, https://doi.org/10.1029/2006wr005631, 2007a.

Leijnse, H., Uijlenhoet, R., and Stricker, J. N. M.: Hydrometeorological application of a microwave link: 1. Evaporation, Water Resources 595 Research, 43, https://doi.org/10.1029/2006wr004988, 2007b.

Leijnse, H., Uijlenhoet, R., and Stricker, J. N. M.: Hydrometeorological application of a microwave link: 2. Precipitation, Water Resources Research, 43, https://doi.org/10.1029/2006wr004989, 2007c.

Leijnse, H., Uijlenhoet, R., and Stricker, J. N. M.: Microwave link rainfall estimation: Effects of link length and frequency, temporal sampling, power resolution, and wet antenna attenuation, Advances in Water Resources, 31, 1481–1493, 600 https://doi.org/10.1016/j.advwatres.2008.03.004, 2008.

Lüdi, A., Beyrich, F., and Mätzler, C.: Determination of the Turbulent Temperature–Humidity Correlation from Scintillometric Measurements, Boundary-Layer Meteorology, 117, 525–550, https://doi.org/10.1007/s10546-005-1751-1, 2005.

Medeiros Filho, F., Jayasuriya, D., Cole, R., and Helmis, C.: Spectral density of millimeter wave amplitude scintillations in an absorption region, IEEE Transactions on Antennas and Propagation, 31, 672–676, https://doi.org/10.1109/TAP.1983.1143111, 1983.

605 Meijninger, W., Green, A., Hartogensis, O., Kohsiek, W., Hoedjes, J., Zuurbier, R., and De Bruin, H.: Determination of area-averaged water vapour fluxes with large aperture and radio wave scintillometers over a heterogeneous surface–Flevoland field experiment, Boundary-Layer Meteorology, 105, 63–83, https://doi.org/10.1023/A:1019683616097, 2002.

Meir, P. and Woodward, F. I.: Amazonian rain forests and drought: response and vulnerability, New Phytol, 187, 553–7, https://doi.org/10.1111/j.1469-8137.2010.03390.x, 2010.

610 Messer, H., Zinevich, A., and Alpert, P.: Environmental monitoring by wireless communication networks, Science, 312, 713, https://doi.org/10.1126/science.1120034, 2006.

Mu, Q., Heinsch, F. A., Zhao, M., and Running, S. W.: Development of a global evapotranspiration algorithm based on MODIS and global meteorology data, Remote Sensing of Environment, 111, 519–536, https://doi.org/10.1016/j.rse.2007.04.015, 2007.

Ostrometzky, J., Eshel, A., Alpert, P., and Messer, H.: Induced bias in attenuation measurements taken from commercial microwave links, in: 2017 IEEE International Conference on Acoustics, Speech and Signal Processing (ICASSP), pp. 3744–3748, ISBN 2379-190X, https://doi.org/10.1109/ICASSP.2017.7952856, 2017.

Ruisdael Observatory: Ruisdael Observatory, https://ruisdael-observatory.nl/cabauw/ [Accessed: 01-04-2024], 2024.

Seneviratne, S. I., Corti, T., Davin, E. L., Hirschi, M., Jaeger, E. B., Lehner, I., Orlowsky, B., and Teuling, A. J.: Investigating soil moisture–climate interactions in a changing climate: A review, Earth-Science Reviews, 99, 125–161, 620 https://doi.org/10.1016/j.earscirev.2010.02.004, 2010.

Stull, R.: An Introduction to Boundary Layer Meteorology, Atmospheric and Oceanographic Sciences Library, Springer Netherlands, ISBN 9789027727695, 1988.

Su, Z.: The Surface Energy Balance System (SEBS) for estimation of turbulent heat fluxes, Hydrol. Earth Syst. Sci., 6, 85–100, https://doi.org/10.5194/hess-6-85-2002, hESS, 2002.

625 Tatarskii, V. I.: The effects of the turbulent atmosphere on wave propagation, Jerusalem: Israel Program for Scientific Translations, 1971, https://articles.adsabs.harvard.edu/pdf/1971etaw.book.....T, 1971.

Tatarskiĭ, V.: Wave Propagation in a Turbulent Medium, McGraw-Hill, New York, 1961.

Tunick, A.: C_n^2 model to calculate the micrometeorological influences on the refractive index structure parameter, Environmental Modelling & Software, 18, 165–171, https://doi.org/10.1016/s1364-8152(02)00052-x, 2003.

630 Van de Boer, A., Moene, A. F., Graf, A., Simmer, C., and Holtslag, A. A.: Estimation of the refractive index structure parameter from single-level daytime routine weather data, Appl Opt, 53, 5944–60, https://doi.org/10.1364/AO.53.005944, 2014.

van der Valk, L. D., Coenders-Gerrits, M., Hut, R. W., Overeem, A., Walraven, B., and Uijlenhoet, R.: Measuring rainfall using microwave links: the influence of temporal sampling, Atmospheric Measurement Techniques, 17, 2811–2832, https://doi.org/10.5194/amt-17-2811-2024, 2024a.

635 van der Valk, L. D., Hartogensis, O. K., Coenders-Gerrits, M., Hut, R. W., Walraven, B., and Uijlenhoet, R.: Dataset: Use of commercial microwave links as scintillometers, https://doi.org/10.4121/247d47b7-2ea5-4e93-bffb-67620a66525c, 2024b.

van Dinther, D.: Measuring crosswind using scintillometry, Wageningen University and Research, ISBN 9798708785961, 2015.

van Leth, T. C., Overeem, A., Leijnse, H., and Uijlenhoet, R.: A measurement campaign to assess sources of error in microwave link rainfall estimation, Atmospheric Measurement Techniques, 11, 4645–4669, https://doi.org/10.5194/amt-11-4645-2018, 2018.

640 Villarreal, S. and Vargas, R.: Representativeness of FLUXNET sites across Latin America, Journal of Geophysical Research: Biogeosciences, 126, https://doi.org/10.1029/2020jg006090, 2021.

Wang, K. and Dickinson, R. E.: A review of global terrestrial evapotranspiration: Observation, modeling, climatology, and climatic variability, Reviews of Geophysics, 50, https://doi.org/10.1029/2011rg000373, 2012.

Wang, T.-i., Ochs, G., and Clifford, S.: A saturation-resistant optical scintillometer to measure C_n^2, Journal of the Optical Society of America, 645 68, 334–338, https://doi.org/10.1364/JOSA.68.000334, 1978.

Ward, H. C., Evans, J. G., Hartogensis, O. K., Moene, A. F., De Bruin, H. A. R., and Grimmond, C. S. B.: A critical revision of the estimation of the latent heat flux from two-wavelength scintillometry, Quarterly Journal of the Royal Meteorological Society, 139, 1912–1922, https://doi.org/10.1002/qj.2076, 2013.

650   Ward, H. C., Evans, J. G., Grimmond, C. S. B., and Bradford, J.: Infrared and millimetre-wave scintillometry in the suburban environment – Part 1: Structure parameters, Atmospheric Measurement Techniques, 8, 1385–1405, https://doi.org/10.5194/amt-8-1385-2015, 2015.

West, H., Quinn, N., and Horswell, M.: Remote sensing for drought monitoring & impact assessment: Progress, past challenges and future opportunities, Remote Sensing of Environment, 232, https://doi.org/10.1016/j.rse.2019.111291, 2019.

Wyngaard, J. C., Izumi, Y., and Collins, S. A.: Behavior of the refractive-index-structure parameter near the ground, Journal of the Optical Society of America, 61, 1646–1650, https://doi.org/10.1364/JOSA.61.001646, 1971.